Article

Not peer-reviewed version

Stellar Stability Vector Space: Stability Gates, Homeostatic Windows, and Time-Weighted Ripeness in Kepler–Gaia Dwarfs

Stephen Atalebe *

Posted Date: 19 March 2026

doi: 10.20944/preprints202603.1518.v1

Keywords: stellar rotation; gyrochronology; Kepler; Gaia; statistical classification; stability; residence time

 doi:10.20944/preprints202603.1518.v1

Article

Stellar Stability Vector Space: Stability Gates, Homeostatic Windows, and Time-Weighted Ripeness in Kepler–Gaia Dwarfs

Stephen Atalebe

Masaryk University, Czech Republic; 478944@muni.cz

Abstract

Stellar stability is typically characterized by instantaneous structural parameters, while age is treated as an external attribute. This work tests whether a class-conditioned stability space can be operationalized such that bounded basin membership and extremal subsets couple to residence time. A Kepler–Gaia dwarf sample is constructed and a temperature-binned stability gate is identified in $\log_{10} P_{\rm rot}$ using a two-component Gaussian mixture model. Within the gated sample, a bounded homeostatic window is defined in a scalar potential $\Phi_\star$. Gyro ages are obtained for 6447/7366 post-gate stars (87.5% coverage), spanning 1.51–13.77 Gyr (median 5.10 Gyr). In the pooled sample, window members are older than non-members with $\Delta\tilde{t} = +0.316$ Gyr (Kolmogorov–Smirnov $p = 8.24 \times 10^{-59}$). Per-bin time-weighted ripeness tails isolate older subsets in the 4000–5200 K and 5200–6000 K regimes. A residualized permutation null that removes temperature-bin geometry yields an empirical $p \simeq 0.002$, supporting within-bin time coupling beyond bin composition. A scaling variance tests was used to evaluate whether the stability coordinate exhibits non-random organisation that persists under progressive coarse-graining.

Keywords: stellar rotation; gyrochronology; Kepler; Gaia; statistical classification; stability; residence time

1. Introduction

Stellar characterization is usually built from instantaneous parameters such as effective temperature, surface gravity, and metallicity, while stability and age are treated as separate attributes. Rotation provides a direct long-baseline tracer of regulation because magnetic braking produces systematic spin-down with time, beginning with the classic $P \propto t^{1/2}$ scaling [1], and later extensions that formalize rotational evolution across mass and age [2]. This work adopts a complementary operational view: stability is treated as a *state of residence*. If a star occupies a regulated configuration for long durations, that duration should be part of the stability definition, not an optional annotation.

This perspective is motivated by problems where long-lived, low-hazard stellar output matters, including long-term climate maintenance and long-horizon habitability screening for rocky planets [3,4]. The focus here is not habitability modelling, but the upstream stellar classification problem: how to define a reproducible, class-conditioned stability space and then test whether that space couples to a time coordinate. The novelty of this work is not gyrochronology itself, but the operational definition of a class-conditioned stability basin and the demonstration that its bounded core and extremal tails couple to residence time beyond bin-composition effects.

1.1. Problem Statement

The technical challenge is to construct a reproducible, class-conditioned state space in which a bounded homeostatic region can be defined, then test whether membership and extremal subsets of that region couple to a measurable time coordinate. Rotation is central because it is both observable at scale in Kepler light curves and physically tied to angular momentum loss and magnetic activity evolution [5].

 doi:10.20944/preprints202603.1518.v1

1.2. Homeostatic Window and Time-Weighted Ripeness

A homeostatic window is defined here as a bounded basin core in a scalar potential $\Phi_\star$ derived from a class-normalized state vector. Ripeness is defined as a time-weighted functional: high ripeness corresponds to long residence times in the regulated basin. The same bounded-window plus residence-time logic is intended to be portable to other astrophysical systems where transitions and residence times can be operationalized.

1.3. Hypotheses and Falsifiers

Four hypotheses guide the tests.

- H1 (bounded window): a bounded homeostatic window exists within well-defined stellar classes.
- H2 (large-N separability): window membership is detectable at scale after class conditioning.
- H3 (ripeness coupling): time-weighted ripeness is coupled to a time coordinate, and is not an instantaneous score.
- H4 (stability gate): a stability gate separates a fast-rotator peak from a regulated slow-rotator peak.

These hypotheses are falsified if the window collapses under modest perturbations of the bounds, if the gate disappears under class conditioning, if the window versus non-window age contrast is consistent with permutation nulls, or if signals strengthen only through selection effects rather than reproducible conditioning and robustness checks.

1.4. Outline

Section 2 describes the Kepler rotation catalog and Gaia DR3 inputs and the cross-match strategy. Section 3 defines the GMM stability gate, the scalar potential $\Phi_\star$, the bounded window, gyrochronology ages, and the time-weighted ripeness functional. Section 4 reports window statistics, gyro-age validation of H3, and permutation-based robustness checks, including a drilldown of the cool-dwarf regime. Section 6 interprets the results physically, clarifies selection effects in external age catalogs, and summarizes limitations and next steps.

2. Data

The analysis combines Kepler rotation periods from McQuillan et al. [5] with Gaia DR3 astrometric and photometric parameters [6]. These identifiers are mapped to Gaia DR3 `source_id` using a published KIC–Gaia cross-match table [7]. The working sample is restricted to main-sequence dwarfs and is temperature-binned to reduce population mixing and to keep the gate inference local in stellar type.

2.1. Kepler Rotation Periods

The McQuillan et al. catalog provides rotation periods for 34030 Kepler targets derived from photometric modulation [5]. These periods are the primary observable for gate detection and for gyrochronology age inference.

2.2. Gaia DR3 Parameters and Quality Control

Gaia DR3 provides astrometry and photometry used to construct the state vector and to estimate colors for gyrochronology [6]. Inputs include G-band photometry, BP–RP color, parallax, and solution quality metrics. A conservative quality filtering is applied to reduce contamination from problematic astrometric solutions, and only rows with finite inputs required for the Tier-1 potential are retained.

2.3. KIC to Gaia DR3 Cross-Match

Kepler targets are indexed by KIC identifiers. These identifiers are mapped to Gaia DR3 `source_id` using a published KIC–Gaia cross-match table (Table A1 in Godoy-Rivera et al.; used as a deterministic mapping for large N). For calibration subsets where KIC or `source_id` ambiguities may exist, direct cone searches against the ESA Gaia archive provide a validation and fallback mapping step.

 doi:10.20944/preprints202603.1518.v1

2.4. Pipeline Attrition Summary

Table 1 summarizes sample sizes across the main pipeline stages. The post-gate sample size $N = 7366$ is the primary working sample for windowing and ripeness inference.

Table 1. Sample sizes across the main pipeline stages. "Kepler–Gaia merged" denotes targets with a mapped Gaia DR3 `source_id` and finite Tier-1 inputs after quality filtering. "Post-gate" denotes the slow-rotator peak retained by the per-bin GMM stability gate.

Stage	N	Description
McQuillan rotators [5]	34030	Kepler rotation periods
KIC→Gaia mapping available	33870	Unique Gaia `source_id` values after mapping
Kepler–Gaia merged (quality filtered)	16635	Finite BP–RP, parallax, and period inputs
Post-gate (GMM slow peak)	7366	Regulated slow-rotator population
With gyro ages (Mamajek)	6447	Finite gyro ages after model-domain filters

3. Methods

3.1. Stability Gate from a Gaussian Mixture Model

For each temperature bin, a two-component Gaussian mixture model is fit to $\log_{10} P_{\rm rot}$ to separate a fast-rotator peak from a regulated slow-rotator peak. The gate period $P_{\rm gate}^{\rm GMM}$ is defined as the midpoint between the two component means in $\log_{10} P_{\rm rot}$ space. This uses rotation-period structure directly, without external age labels [1,2]. Post-gate membership is defined as

$$R_{\rm raw}^{\rm GMM} \equiv \log_{10} P_{\rm rot} - \log_{10} P_{\rm gate}^{\rm GMM} \geq 0, \tag{1}$$

so only the slow side is retained for subsequent windowing.

3.2. Homeostatic Potential and Robust Normalization

A Tier-1 state space is defined from two high-coverage proxies: a regulation coordinate derived from rotation relative to the gate and a forcing coordinate derived from absolute magnitude. The raw proxies are

$$R_{\rm raw} \equiv \log_{10} P_{\rm rot} - \log_{10} P_{\rm gate}^{\rm GMM}, \qquad H_{\rm raw} \equiv -M_G. \tag{2}$$

Within each temperature bin, robust normalization uses the median and median absolute deviation (MAD),

$$\hat{X} = \frac{X - \mathrm{median}(X)}{\mathrm{MAD}(X)}, \tag{3}$$

with $X \in \{R_{\rm raw}, H_{\rm raw}\}$. The scalar homeostatic potential is defined as

$$\Phi_\star \equiv \hat{R} + \hat{H}, \tag{4}$$

corresponding to locked weights $(w_R, w_H, w_M, w_S) = (1, 1, 0, 0)$ in the more general four-component formalism. Additional components are treated as Tier escalation because stable, high-coverage proxies are not yet integrated into the large-N Kepler–Gaia build.

For notational convenience in the variance-scaling section, define $\Phi_{\rm gmm} \equiv \Phi_\star$ for the post-gate sample.

3.3. Bounded Homeostatic Window

Window membership is defined as a bounded quantile slice of $\Phi_\star$ within each temperature bin,

$$Q_{0.35}(\Phi_\star) \leq \Phi_\star \leq Q_{0.65}(\Phi_\star), \tag{5}$$

so the window fraction is 30% by construction in each bin.

 doi:10.20944/preprints202603.1518.v1

3.4. Gyrochronology Age Scale

Direct asteroseismic ages are precise but have limited overlap with rotation-selected dwarf samples at scale, motivating a gyrochronology proxy for time weighting. The gyrochronology relation of Mamajek and Hillenbrand [8] is implemented as

$$P = A\,(B-V-C)^{B}\,t^{N}, \tag{6}$$

with t in Myr then converted to Gyr. Constants are $A = 0.407$, $B = 0.325$, $C = 0.495$, $N = 0.566$ [8]. Color $B-V$ is estimated from Gaia BP–RP using a dwarf-regime mapping. The resulting gyro age is denoted t_{gyro}.

3.5. Time-Weighted Ripeness and Tails

Time-weighted ripeness is defined as

$$R_{\mathrm{ripe}}^{\mathrm{time}} \equiv \Phi_{\star}\, t_{\mathrm{gyro}}, \tag{7}$$

computed only where t_{gyro} is finite. Three tail definitions separate absolute and regime-relative questions.

- Global post-gate tails: top 10% and top 5% of $R_{\mathrm{ripe}}^{\mathrm{time}}$ across all post-gate stars.
- Within-window tails: top 10% and top 5% of $R_{\mathrm{ripe}}^{\mathrm{time}}$ within the window cohort.
- Per-bin within-window tails: top 10% and top 5% within the window cohort, computed separately in each temperature bin.

The per-bin within-window tails are used for cross-regime comparison.

3.6. Statistics

Window age separation uses the two-sample Kolmogorov–Smirnov test and a one-sided Mann–Whitney test for the alternative "window older than non-window". Rank coupling uses Kendall τ [9]. Permutation nulls are reported as empirical one-sided probabilities $P(\mathrm{null} \geq \mathrm{obs})$ with +1 smoothing. Two nulls are used.

A residualized null subtracts bin medians from age and $\Phi_{\star}$, then permutes age residuals within bins. A window-age null permutes ages within bins while holding window membership fixed, then recomputes $\Delta\tilde{t} \equiv \tilde{t}_{\mathrm{win}} - \tilde{t}_{\mathrm{non}}$.

4. Results

4.1. Gate and Post-Gate Sample Size

After Gaia validity filtering and initial conditioning, the Kepler-led dataset contains $N = 16635$ stars. Applying the per-bin GMM gate yields $N = 7366$ post-gate stars with bin counts $N_{3200\text{–}4000} = 589$, $N_{4000\text{–}5200} = 2929$, $N_{5200\text{–}6000} = 3020$, $N_{6000\text{–}7500} = 828$. The inferred gate periods shift monotonically to shorter periods at higher temperature, consistent with temperature-dependent rotation distributions [2,5].

4.2. Homeostatic Window Size

Applying Equation (5) yields an anchor window of $N_{\mathrm{win}} = 2210$ (30.003%) across the post-gate sample, with 30% fraction per bin by construction. Table 2 summarizes window counts.

 doi:10.20944/preprints202603.1518.v1

Table 2. Post-gate sample size and homeostatic window counts by temperature bin.

Temperature bin (K)	N_{post}	N_{win}	Window fraction
3200–4000	589	177	0.300
4000–5200	2929	879	0.300
5200–6000	3020	906	0.300
6000–7500	828	248	0.300
Total	7366	2210	0.300

4.3. Ripe Tail Cohort Sizes

Global post-gate tails contain $N_{90} = 737$ (top 10%) and $N_{95} = 370$ (top 5%). Per-bin within-window tails contain $N_{90} = 222$ and $N_{95} = 112$, ensuring regime-relative representation. These cohorts are exported for downstream use.

Table 3. Global post-gate tail sizes by temperature bin. Tail definitions use per-bin quantiles of $\Phi_\star$ and are not window restricted.

Bin (K)	Tail_{90}	Tail_{95}	N_{post}	Tail fractions
3200–4000	59	30	589	0.10, 0.05
4000–5200	293	147	2929	0.10, 0.05
5200–6000	302	151	3020	0.10, 0.05
6000–7500	83	42	828	0.10, 0.05
Total	737	370	7366	0.10, 0.05

4.4. Gyro Ages, Coverage, and Global Summary

Gyro ages from Equation (6) are available for $N = 6447$ of $N = 7366$ post-gate stars (87.5% coverage). The age range is 1.513 to 13.770 Gyr with median 5.098 Gyr. The homeostatic potential spans $\Phi_\star \in [-11.533, 39.009]$ with median 0.216. Time-weighted ripeness spans $[-39.063, 267.320]$ with median 0.458. Table 4 reports global summaries.

Table 4. Global summary statistics for gyro age, $\Phi_\star$, and time-weighted ripeness.

Quantity	N	min	median	max
t_{gyro} (Gyr)	6447	1.513	5.098	13.770
$\Phi_\star$	7366	−11.533	0.216	39.009
$R_{\mathrm{ripe}}^{\mathrm{time}} = \Phi_\star t_{\mathrm{gyro}}$	6447	−39.063	0.458	267.320

4.5. H3, Gyro-Age Ripeness Validation

H3 is supported if window members are older than non-members and if per-bin ripeness tails isolate the oldest subsets. Across the pooled sample with gyro ages, window stars are older, $N_{\mathrm{win}} = 2007$ and $N_{\mathrm{non}} = 4440$ with median ages 5.239 Gyr and 4.924 Gyr, giving $\Delta\tilde{t} = +0.316$ Gyr. The shift is strong (KS $p = 8.24 \times 10^{-59}$, one-sided MW $p = 7.08 \times 10^{-10}$). Rank coupling is strong, Kendall $\tau(t_{\mathrm{gyro}}, \Phi_\star) = 0.564$ and $\tau(t_{\mathrm{gyro}}, R_{\mathrm{ripe}}^{\mathrm{time}}) = 0.556$ [9].

Table 5 summarizes per-bin window shifts and per-bin tail age shifts. In 4000–5200 K and 5200–6000 K, window stars are older and both q90 and q95 tails are older than the remainder of each bin. In 6000–7500 K, window stars are older but tail tests are limited by small N. In 3200–4000 K, the window is slightly younger, but the q90 tail is older, indicating that basin-core selection and oldest-star selection are not identical operations in the cool-dwarf regime.

 doi:10.20944/preprints202603.1518.v1

Table 5. H3 gyro-age tests by temperature bin. $\Delta\tilde{t}_{\rm win} = \tilde{t}_{\rm win} - \tilde{t}_{\rm non}$. Tail deltas compare tail median age to non-tail median age within the bin, using per-bin within-window tails where available. MW p is one-sided for "A older than B".

Bin (K)	$N_{\rm age}$	$\tilde{t}_{\rm gyro}$	$\Delta\tilde{t}_{\rm win}$	KS $p_{\rm win}$	MW $p_{\rm win}$	Tail $\Delta\tilde{t}$ (q90, q95)
3200–4000	589	4.439	−0.216	6.89×10^{-3}	0.953	+1.120, +1.647 (q95 small N)
4000–5200	2903	5.102	+0.216	1.20×10^{-43}	1.98×10^{-2}	+0.571, +0.722
5200–6000	2750	5.279	+0.439	2.96×10^{-29}	1.37×10^{-7}	+1.406, +1.558
6000–7500	205	4.695	+1.100	1.12×10^{-2}	3.61×10^{-4}	+3.358, +3.993 (tails small N)

4.6. Null Tests and Robustness

4.6.1. Age Clipping Robustness

A robustness run clipped $t_{\rm gyro} \leq 13.8$ Gyr and recomputed $R_{\rm ripe}^{\rm time}$. The raw maximum is 13.77 Gyr, so clipping produces identical results.

4.6.2. Residualized Permutation Null

A within-bin null removes temperature-bin geometry by residualizing age and $\Phi_\star$ within bins (subtracting bin medians). Age residuals are permuted within bins and residual ripeness is recomputed as $\Phi'_\star\, t'_{\rm gyro}$. Observed residualized rank coupling exceeds the null; the empirical one-sided probability is $p \simeq 0.002$.

4.6.3. Window-Age Permutation Null

A second null permutes ages within bins while holding window membership fixed, then evaluates $\Delta\tilde{t}$. The pooled observed $\Delta\tilde{t} = +0.3159$ Gyr is extreme relative to the null distribution, empirical one-sided $p = 0.0010$.

Table 6. Permutation null summaries for H3 robustness. Empirical p values are one-sided $P(\text{null} \geq \text{obs})$ with +1 smoothing.

Test statistic	Observed	Empirical p
Residualized rank coupling (age vs $\Phi_\star$)	strong	0.0020
Residualized rank coupling (age vs $R_{\rm ripe}^{\rm time}$)	strong	0.0020
Window-age $\Delta\tilde{t}$ pooled (Gyr)	+0.3159	0.0010

4.7. Cool Dwarf Anomaly Drilldown

In 3200–4000 K, the window cohort is slightly younger than the non-window cohort, $\Delta\tilde{t} = -0.216$ Gyr. Two checks show the anomaly persists after stratifying by BP–RP deciles and is reproduced by a Prot-only proxy, indicating a rotation-period composition effect rather than a color composition effect. This regime-dependent behaviour highlights that basin-core selection and maximal residence-time selection are not strictly equivalent operations in low-mass dwarfs.

Table 7. Robustness checks for the 3200–4000 K window age anomaly. The one-sided p column supports "window older".

Test	$N_{\rm win}$	$N_{\rm non}$	$\Delta\tilde{t}$ or Δmedian	p (supports window older)
BP–RP stratified pooled age	168	362	−0.220 Gyr	0.959
Prot-only proxy, $z[\log_{10} P_{\rm rot}]$	177	412	−0.130	0.983

5. Variance Scaling Under Stellar Coarse-Graining

Variance-scaling diagnostics are implemented as a stellar analogue of coarse-graining tests used in other contexts, with a within-bin permutation null that preserves marginal distributions while destroying alignment between the stability coordinate and the coarse-graining axis.

 doi:10.20944/preprints202603.1518.v1

5.1. Colour Coarse-Graining in Gaia bp_rp

Within each `teff_bin_s`, stars are partitioned into K equal-occupancy quantile sub-bins in Gaia colour bp_rp, with $K \in \{5, 10, 20, 40\}$. For each colour sub-bin c, the within-sub-bin variance of $\Phi_{\rm gmm}$ is computed, together with a robust proxy MAD^2. The coarse-graining scale is summarized by the mean colour width $\overline{\Delta \mathrm{bp\_rp}}$.

To reduce leakage from smooth colour trends, a detrended coordinate is used. Within each `teff_bin_s`, stars are ordered by bp_rp and a rolling-median smoother estimates $\widehat{\Phi}(\mathrm{bp\_rp})$ using fractional window frac $= 0.15$. Define

$$\phi_{\rm det} \;=\; \Phi_{\rm gmm} \;-\; \widehat{\Phi}(\mathrm{bp\_rp}). \tag{8}$$

A within-bin permutation null is generated by permuting $\Phi_{\rm gmm}$ within each `teff_bin_s`, then recomputing $\widehat{\Phi}$, $\phi_{\rm det}$, and the quantile coarse-graining. This preserves the marginal $\Phi_{\rm gmm}$ distribution within each temperature bin while destroying any structured alignment with bp_rp.

Table 8 summarizes the two dominant temperature bins. In both bins, the observed coarse-grained variances are systematically below the permutation baseline across K, consistent with within-bin organisation of the stability coordinate relative to colour.

Table 8. Colour coarse-graining variance scaling summary for the two dominant temperature bins. Values are mean within-sub-bin variances $\overline{\sigma^2}$ across the K bp_rp quantile sub-bins. The detrended coordinate $\phi_{\rm det}$ removes a rolling-median colour trend within each `teff_bin_s` using frac $= 0.15$. The permutation null permutes $\Phi_{\rm gmm}$ within `teff_bin_s`.

`teff_bin_s`	Variant	K	$\overline{\Delta \mathrm{bp\_rp}}$	$\overline{\sigma^2}(\Phi_{\rm gmm})$	$\overline{\sigma^2}(\phi_{\rm det})$
4000–5200	observed	5	0.1901	6.9883	6.8888
4000–5200	null	5	0.1901	8.0618	8.0562
4000–5200	observed	10	0.09495	6.9000	6.8740
4000–5200	null	10	0.09495	8.0541	8.0480
4000–5200	observed	20	0.04737	6.8811	6.8717
4000–5200	null	20	0.04737	8.0489	8.0458
4000–5200	observed	40	0.02350	6.8660	6.8631
4000–5200	null	40	0.02350	8.0519	8.0516
5200–6000	observed	5	0.1033	15.2769	14.9628
5200–6000	null	5	0.1033	16.6242	16.6112
5200–6000	observed	10	0.05161	15.0066	14.9511
5200–6000	null	10	0.05161	16.6251	16.6186
5200–6000	observed	20	0.02576	14.9472	14.9581
5200–6000	null	20	0.02576	16.6167	16.6042
5200–6000	observed	40	0.01282	14.9077	14.9190
5200–6000	null	40	0.01282	16.6686	16.6646

5.2. Rotation-Radius Coarse-Graining in $\log_{10} P_{\rm rot}$

A complementary coarse-graining axis is constructed along rotation period. Within each `teff_bin_s`, define $x = \log_{10} P_{\rm rot}$. For bandwidth h, a local-median smoother $\widehat{\Phi}_h(x)$ is computed for each star using neighbours satisfying $|x_j - x_i| \le h$, with a minimum neighbourhood size $N_{\rm min} = 21$. Residuals are

$$r_h \;=\; \Phi_{\rm gmm} \;-\; \widehat{\Phi}_h(x), \tag{9}$$

and scale-dependent dispersion is summarized by $\mathrm{Var}(r_h)$ and $\mathrm{MAD}^2(r_h)$. The permutation null permutes $\Phi_{\rm gmm}$ within `teff_bin_s` prior to smoothing. The informative regime is small h, where neighbourhoods remain local rather than approaching full-bin coverage. If $\Phi_{\rm gmm}$ is locally organised along rotation, the residual dispersion $\mathrm{Var}(r_h)$, where $r_h = \Phi_{\rm gmm} - \Phi_b^h(x)$, should remain

 doi:10.20944/preprints202603.1518.v1

suppressed at small smoothing bandwidth h and approach the permutation baseline as h approaches full-bin coverage.

Table 9. Rotation-radius coarse-graining at small bandwidths. Residuals are $r_h = \Phi_{\rm gmm} - \widehat{\Phi}_h(\log_{10} P_{\rm rot})$, where $\widehat{\Phi}_h$ is a local median within radius h in $\log_{10} P_{\rm rot}$ (minimum neighborhood size 21). The null permutes $\Phi_{\rm gmm}$ within `teff_bin_s`. Reported $\tilde{N}_{\rm neigh}$ is the median number of neighbors used by the smoother.

`teff_bin_s`	Variant	h	N	$\mathrm{Var}(r_h)$	$\tilde{N}_{\rm neigh}$
3200–4000	observed	0.01	589	1.1383	85.0
3200–4000	observed	0.02	589	1.1595	166.0
3200–4000	observed	0.03	589	1.1656	231.0
3200–4000	observed	0.05	589	1.2555	345.0
3200–4000	observed	0.07	589	1.3299	430.0
3200–4000	observed	0.10	589	1.4923	515.0
3200–4000	null	0.01	589	1.9315	85.0
3200–4000	null	0.02	589	1.9294	166.0
3200–4000	null	0.03	589	1.9465	231.0
3200–4000	null	0.05	589	1.9367	345.0
3200–4000	null	0.07	589	1.9361	430.0
3200–4000	null	0.10	589	1.9410	515.0
4000–5200	observed	0.01	2929	4.0102	385.0
4000–5200	observed	0.02	2929	4.0675	768.0
4000–5200	observed	0.03	2929	4.1229	1146.0
4000–5200	observed	0.05	2929	4.3280	1731.0
4000–5200	observed	0.07	2929	4.6324	2154.0
4000–5200	observed	0.10	2929	5.2190	2611.0
4000–5200	null	0.01	2929	8.0641	385.0
4000–5200	null	0.02	2929	8.0566	768.0
4000–5200	null	0.03	2929	8.0647	1146.0
4000–5200	null	0.05	2929	8.0698	1731.0
4000–5200	null	0.07	2929	8.0718	2154.0
4000–5200	null	0.10	2929	8.0684	2611.0
5200–6000	observed	0.01	3020	5.6009	358.0
5200–6000	observed	0.02	3020	5.6254	702.5
5200–6000	observed	0.03	3020	5.6447	1027.0
5200–6000	observed	0.05	3020	5.7767	1551.0
5200–6000	observed	0.07	3020	5.9997	1974.0
5200–6000	observed	0.10	3020	6.5892	2445.0
5200–6000	null	0.01	3020	16.5789	358.0
5200–6000	null	0.02	3020	16.5761	702.5
5200–6000	null	0.03	3020	16.5809	1027.0
5200–6000	null	0.05	3020	16.5778	1551.0
5200–6000	null	0.07	3020	16.5793	1974.0
5200–6000	null	0.10	3020	16.5952	2445.0
6000–7500	observed	0.01	828	1.9770	50.0
6000–7500	observed	0.02	828	1.9702	100.0
6000–7500	observed	0.03	828	1.9744	147.5
6000–7500	observed	0.05	828	1.9806	239.0
6000–7500	observed	0.07	828	2.0019	326.5
6000–7500	observed	0.10	828	2.0601	438.5
6000–7500	null	0.01	828	6.4841	50.0
6000–7500	null	0.02	828	6.6368	100.0
6000–7500	null	0.03	828	6.6169	147.5
6000–7500	null	0.05	828	6.6219	239.0
6000–7500	null	0.07	828	6.6541	326.5
6000–7500	null	0.10	828	6.6110	438.5

 doi:10.20944/preprints202603.1518.v1

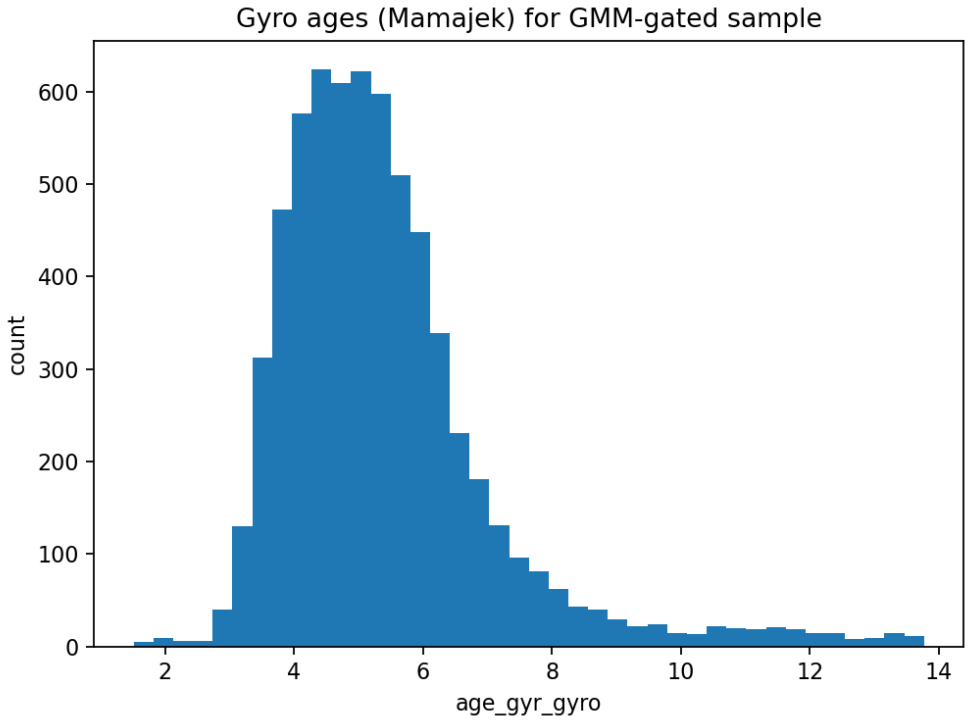

Figure 1. Gyro age distribution for the post gate Kepler–Gaia dwarf sample.

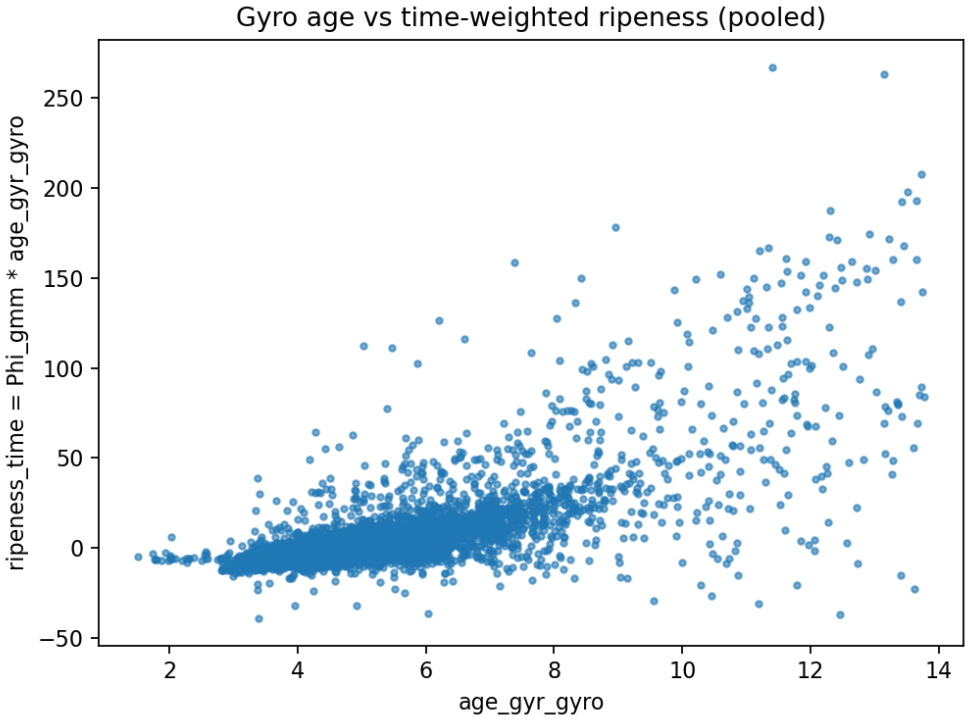

Figure 2. Gyro age versus time weighted ripeness $R_{\rm ripe}^{\rm time} = \Phi_\star t_{\rm gyro}$ for the pooled post gate sample.

 doi:10.20944/preprints202603.1518.v1

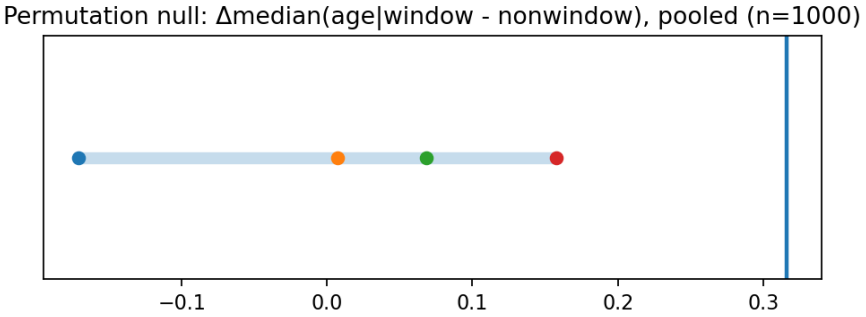

Figure 3. Window age permutation null for the pooled $\Delta\tilde{t}$ statistic.

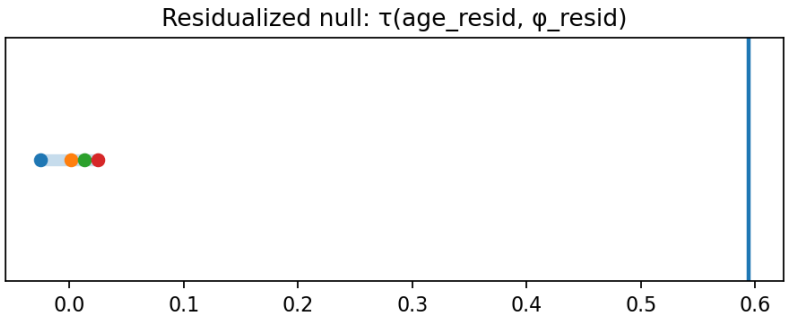

Figure 4. Residualized permutation null for $\tau(t'_{\mathrm{gyro}}, \Phi'_{\star})$, where residuals subtract bin medians.

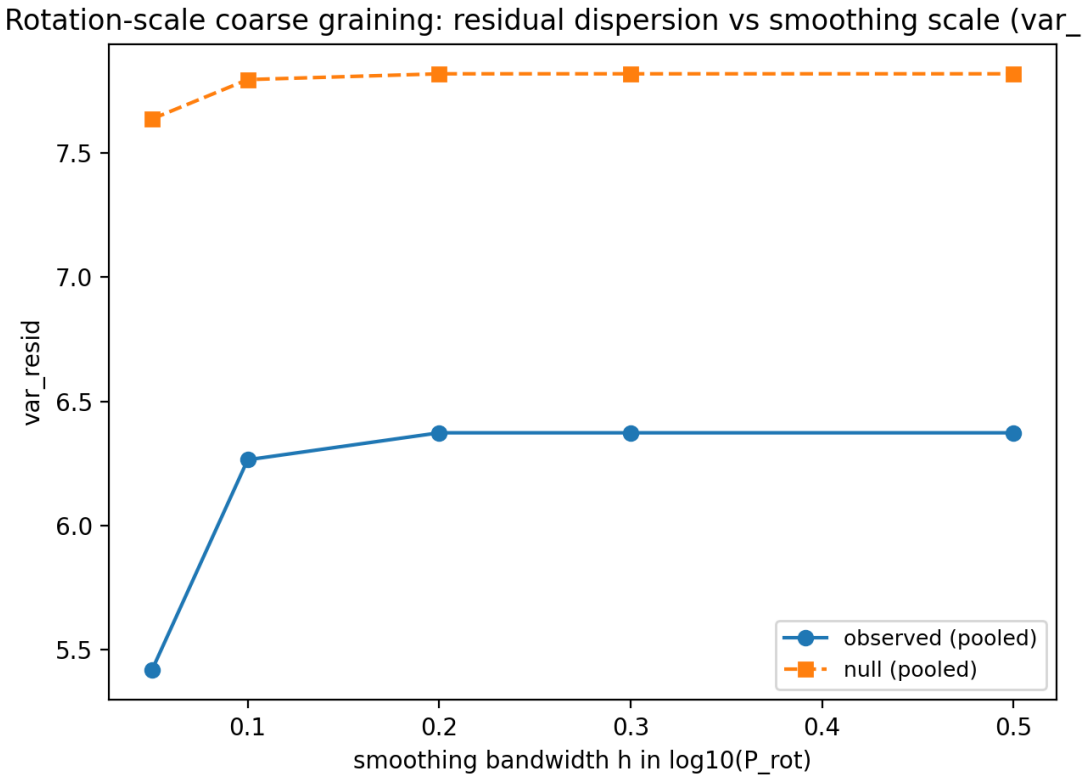

Figure 5. Variance of rotation-smoothing residuals for the pooled sample.

 doi:10.20944/preprints202603.1518.v1

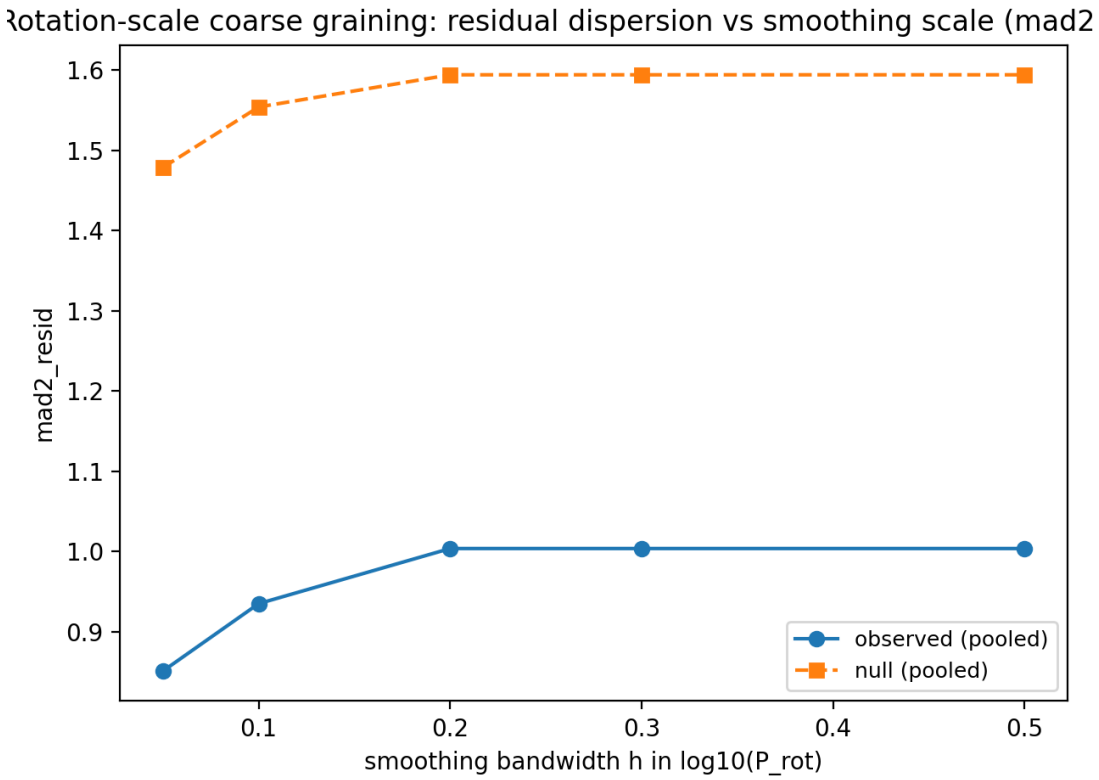

Figure 6. Robust dispersion (MAD^2) of rotation-smoothing residuals for the pooled sample.

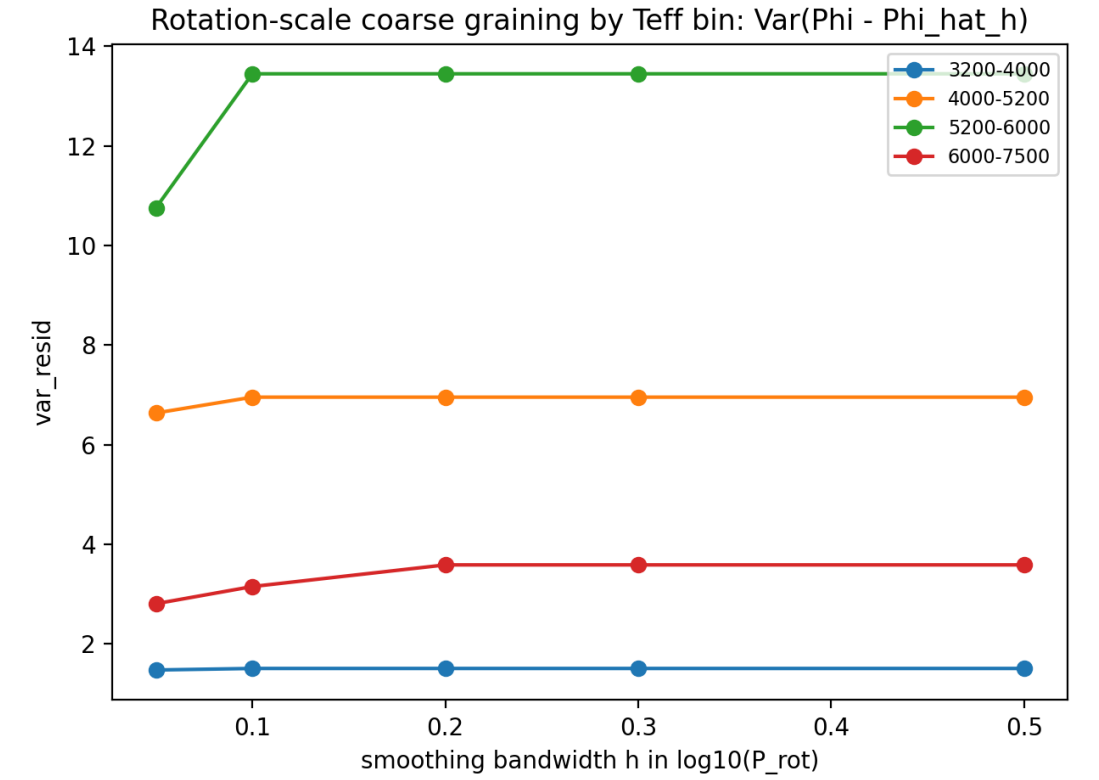

Figure 7. Variance of rotation-smoothing residuals by temperature bin.

 doi:10.20944/preprints202603.1518.v1

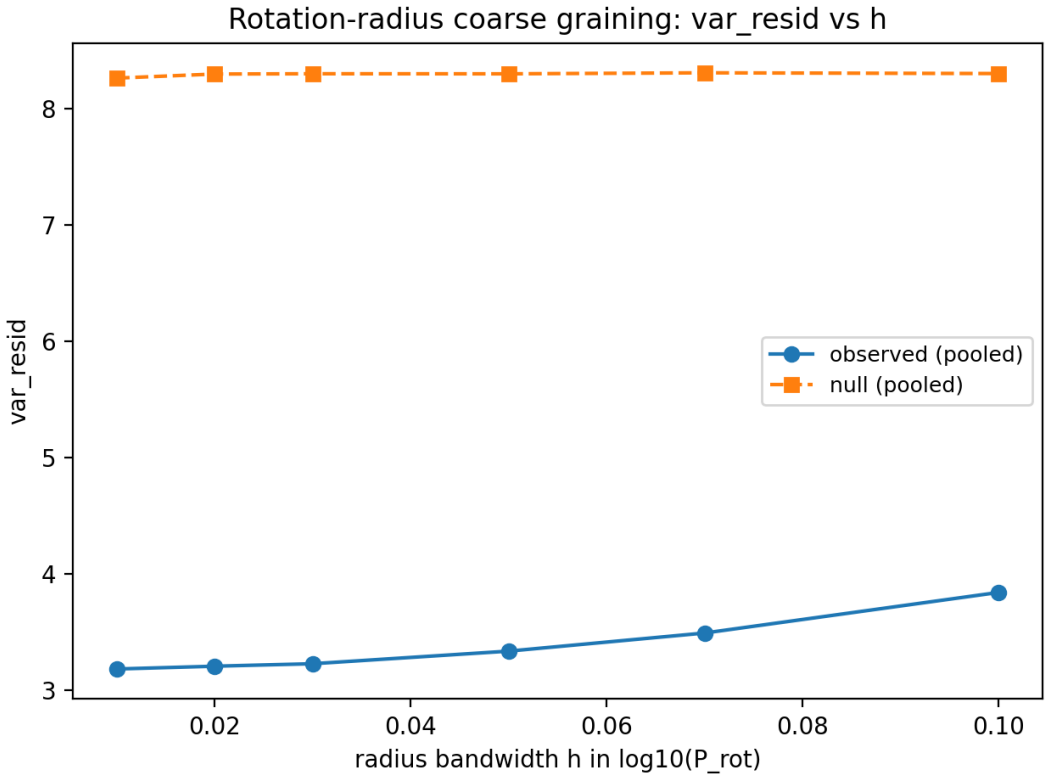

Figure 8. Variance of rotation-radius residuals as a function of bandwidth h for the pooled sample.

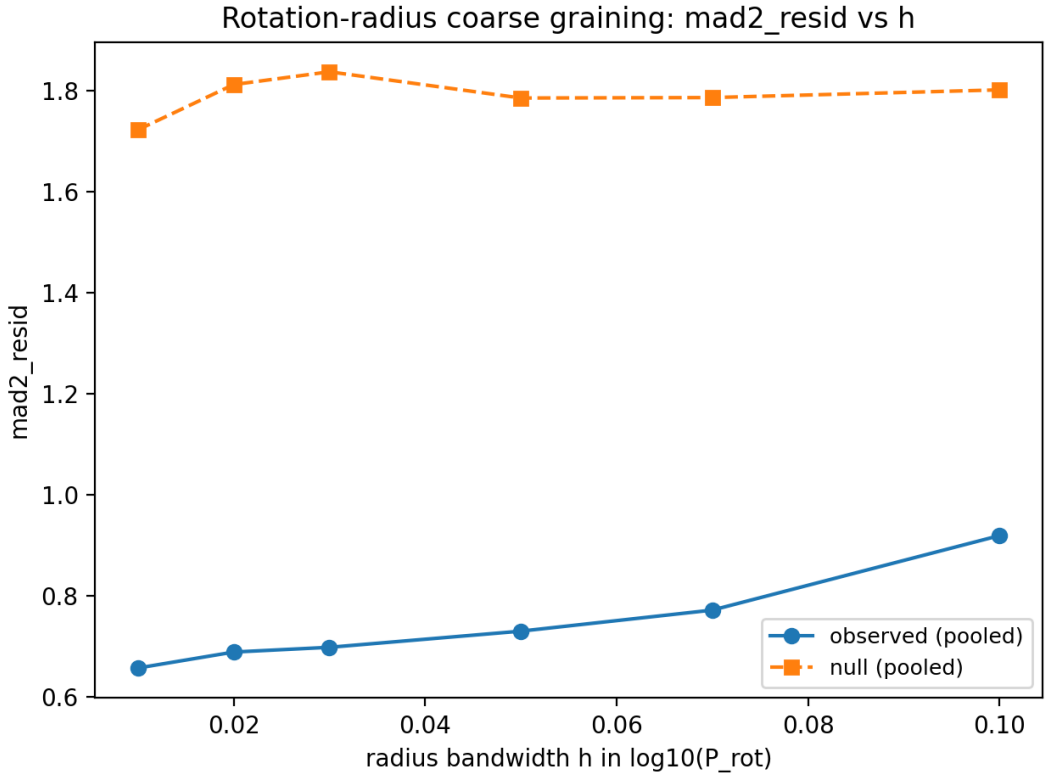

Figure 9. Robust dispersion (MAD^2) of rotation-radius residuals as a function of bandwidth h for the pooled sample.

 doi:10.20944/preprints202603.1518.v1

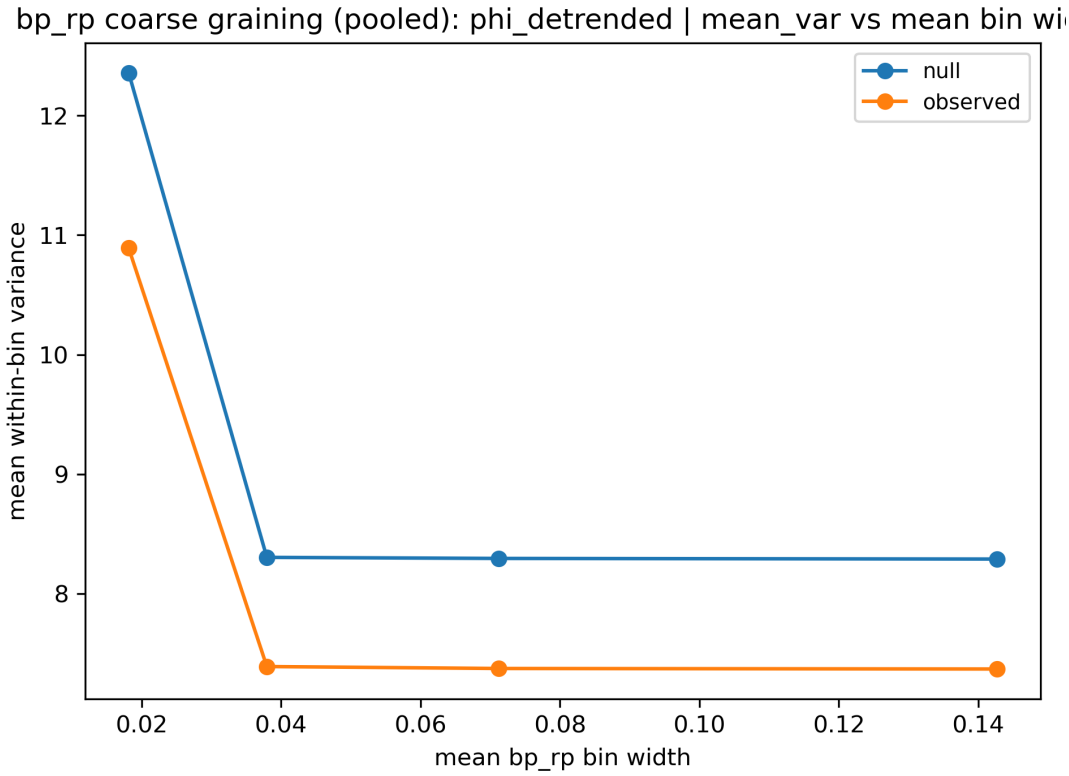

Figure 10. Detrended colour coarse-graining: pooled variance versus mean colour-bin width.

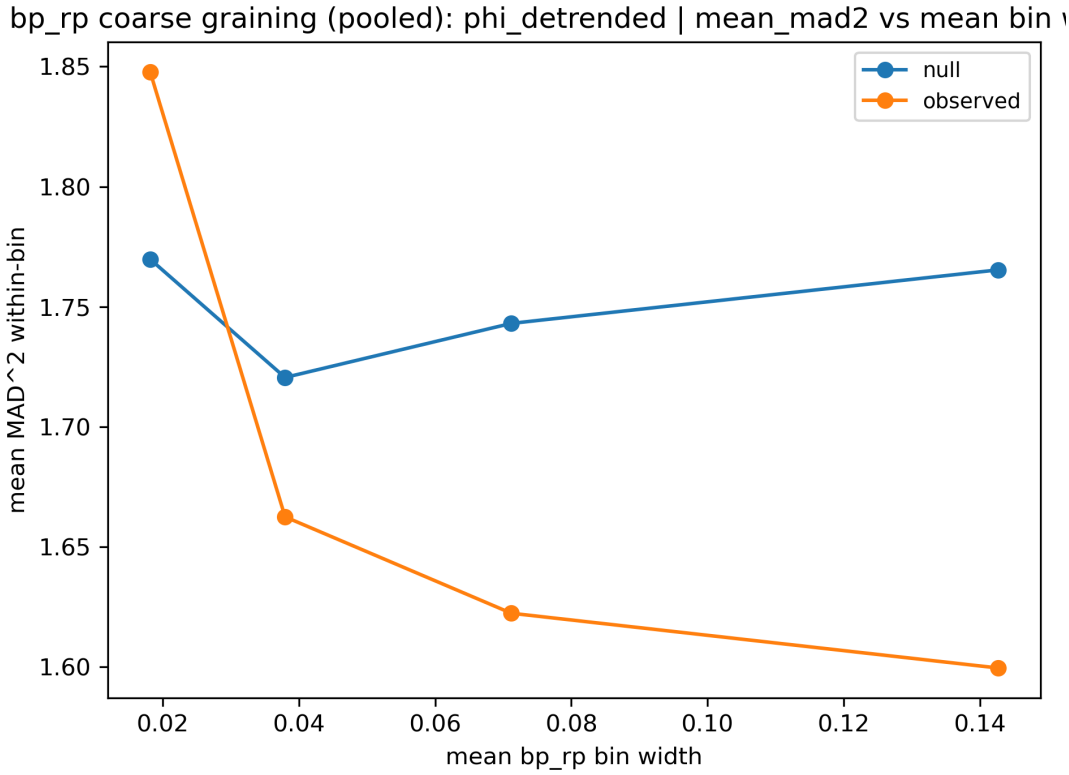

Figure 11. Detrended colour coarse-graining: pooled robust dispersion (MAD^2) versus mean colour-bin width.

 doi:10.20944/preprints202603.1518.v1

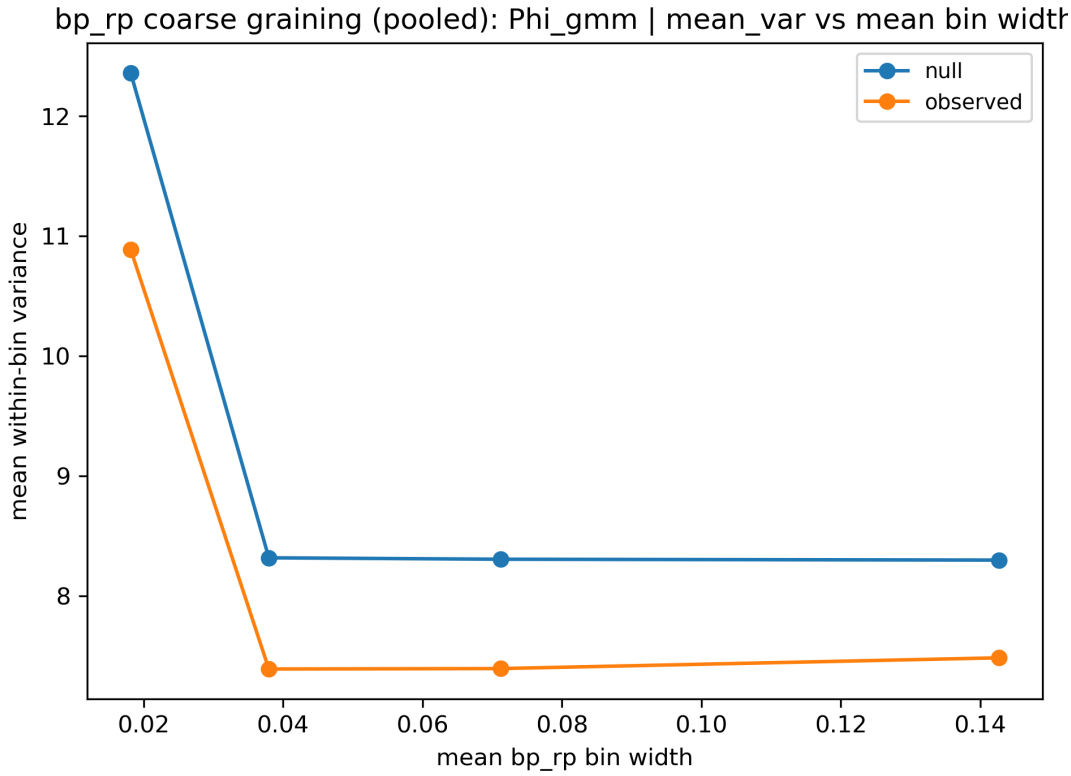

Figure 12. Raw Φ_{gmm} colour coarse-graining: pooled variance versus mean colour-bin width.

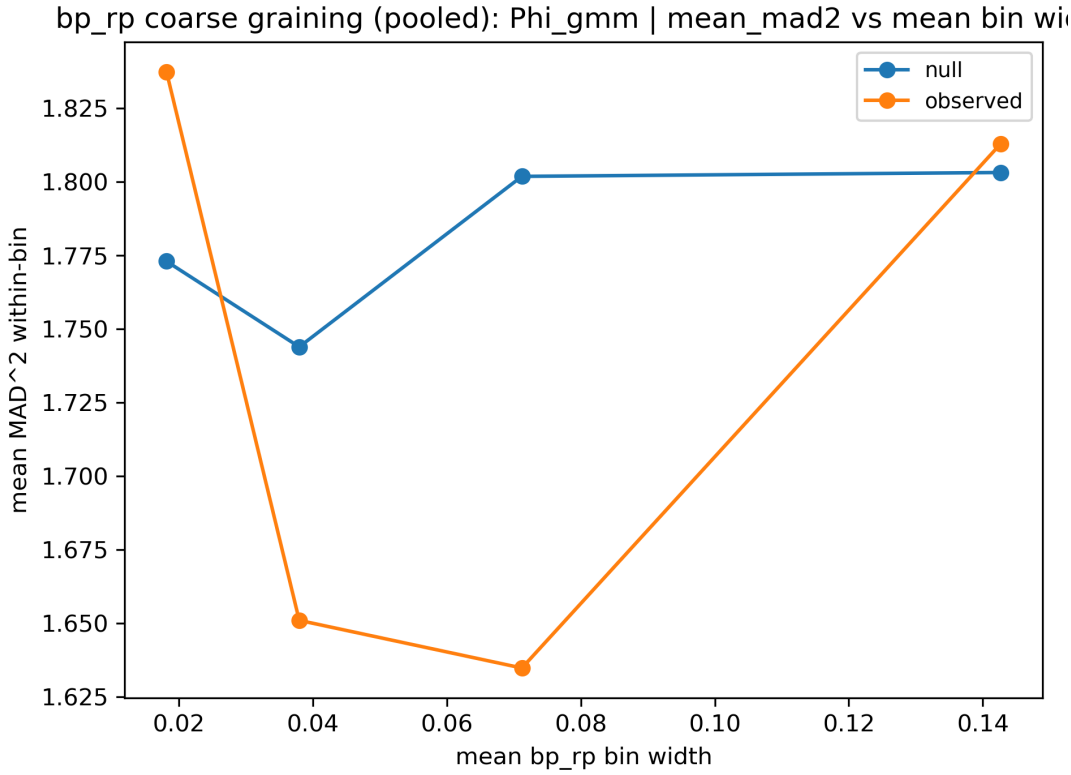

Figure 13. Raw Φ_{gmm} colour coarse-graining: pooled robust dispersion (MAD^2) versus mean colour-bin width.

 doi:10.20944/preprints202603.1518.v1

6. Discussion

6.1. Gate then Window, and What Each Stage Measures

The stability gate is an empirical separation in the rotation-period distribution that isolates a regulated slow peak in each temperature regime. The gate is defined without external age labels and provides a reproducible filtration that removes the fast peak [1,2]. The homeostatic window is a bounded basin core in $\Phi_\star$, not a tail selector. A basin-core cohort serves as a stability-coherence reference set, while a separate ripeness tail cohort serves as a long-residence target list. The cool-bin behaviour shows that basin-core selection and oldest-star selection are not identical operations in every regime.

6.2. Age Catalogs and Validation by Exclusion, with Asteroseismic Casebook

Asteroseismic ages are precise but selection limited for rotation-selected dwarfs. This motivates gyro ages for large-N dwarf time weighting [8]. Even at negligible overlap, a small asteroseismic "casebook" provides a sanity check against independent ages.

Exactly three Kepler LEGACY stars overlap the gated sample. Two are hotter (6000–7500 K) with young ages and short periods and neither enters the global ripeness tail. The third is cooler (4000–5200 K) with an asteroseismic age $t = 9.25$ Gyr and a long period, and it ranks into the top decile of the global ripeness catalog. This supports the operational meaning of time-weighted ripeness.

Table 10. Asteroseismic casebook for the three Kepler LEGACY stars overlapping the GMM-gated sample. The older cool dwarf is ranked into the global top-decile ripeness tail, while the two younger hot stars are not.

Gaia `source_id`	$T_{\rm eff}$ bin	$t_{\rm seis}$ (Gyr)	$P_{\rm rot}$ (d)	$\Phi_{\rm gmm}$	$R^{\rm ripe}$	Tail$_{90}$
2105298788456363008	4000–5200	9.25	35.36	3.58	126.6	yes
2085664985422688896	6000–7500	2.49	12.33	0.37	4.58	no
2078741876099629056	6000–7500	3.19	11.74	−0.66	−7.74	no

6.3. Limitations

Gyro ages have intrinsic scatter and depend on the adopted colour conversion and calibration law [8]. The Mamajek relation has an explicit domain constraint $B-V-C>0$ and is calibrated over a finite colour range. For the reddest targets, BP–RP$\rightarrow B-V$ mappings can saturate, limiting colour leverage and motivating conservative interpretation in the coolest regime. The present $\Phi_\star$ uses two Tier-1 proxies. A full four-component (R, H, M, S) implementation requires stable large-N proxies for hazard and memory and is treated as Tier escalation.

6.4. Next Steps

Immediate extensions include integrating additional dwarf age constraints with meaningful overlap, building an evolved-star branch for direct gyro versus independent-age comparison, and testing window definitions under modest bound perturbations. A second extension is to integrate additional proxies for hazard and memory to expand from a two-axis potential to a four-component potential.

7. Conclusions

A reproducible Kepler–Gaia dwarf pipeline operationalizes a homeostatic window and a time-weighted ripeness functional. A per-bin GMM stability gate isolates a regulated slow-rotator population ($N = 7366$). A bounded window (30% basin core per bin) defines stability-coherence anchors, while high-ripeness tails define extreme residence-time candidates.

Using Mamajek gyrochronology ages, window members are older than non-members in the pooled sample ($\Delta\tilde{t} = +0.316$ Gyr, KS $p = 8.24 \times 10^{-59}$). Per-bin ripeness tails isolate older stars in the dominant temperature regimes. Residualized and window-age permutation nulls yield empirical $p \simeq 0.002$ and $p \simeq 0.001$, supporting within-bin time coupling beyond temperature-bin composition.

 doi:10.20944/preprints202603.1518.v1

A cool-dwarf exception appears at the window level in 3200–4000 K, while the ripeness tail remains older within the same bin.

The exported per-bin tail catalogs provide reproducible target lists for follow-up and cross-matching with exoplanet host samples, where long-term stellar stability is a critical upstream constraint.

Funding: No specific funding was received for this research.

Data Availability Statement: The Kepler rotation catalogs and Gaia DR3 astrometric and photometric data analyzed in this work are publicly available. All code used to construct the Kepler–Gaia dwarf sample, implement the Gaussian mixture stability gate, compute homeostatic potentials, and generate figures and tables is openly available at: https://github.com/Atalebe/Stellar_Homeostatic_Potential_Vector The exported per-bin tail catalogs and variance-scaling outputs are included in that repository. Additional derived data that support the findings of this study can be obtained from the authors upon reasonable request.

Conflicts of Interest: The author declares that there are no financial or personal relationships that could inappropriately influence the work presented in this manuscript.

References

1. Skumanich, A. Time Scales for Ca II Emission Decay, Rotational Braking, and Lithium Depletion. *The Astrophysical Journal* **1972**, *171*, 565–567. https://doi.org/10.1086/151310.
2. Barnes, S.A. Ages for Intermediate-age Open Clusters from Gyrochronology. *The Astrophysical Journal* **2007**, *669*, 1167–1189. https://doi.org/10.1086/519295.
3. Kasting, J.F.; Whitmire, D.P.; Reynolds, R.T. Habitable Zones around Main Sequence Stars. *Icarus* **1993**, *101*, 108–128. https://doi.org/10.1006/icar.1993.1010.
4. Kopparapu, R.K.; Ramirez, R.; Kasting, J.F.; Eymet, V.; Robinson, T.D.; Mahadevan, S.; Terrien, R.C.; Domagal-Goldman, S.; Meadows, V.; Deshpande, R. Habitable Zones around Main-sequence Stars: New Estimates. *The Astrophysical Journal* **2013**, *765*, 131. https://doi.org/10.1088/0004-637X/765/2/131.
5. McQuillan, A.; Mazeh, T.; Aigrain, S. Rotation Periods of 34,030 Kepler Main-sequence Stars: The Full Autocorrelation Sample. *The Astrophysical Journal Supplement Series* **2014**, *211*, 24. https://doi.org/10.1088/0067-0049/211/2/24.
6. Gaia Collaboration.; Brown, A.G.A.; Vallenari, A.; Prusti, T.; de Bruijne, J.H.J.; Babusiaux, C.; Biermann, M.; et al.. Gaia Data Release 3: Summary of the Content and Survey Properties. *Astronomy & Astrophysics* **2023**, *674*, A1. https://doi.org/10.1051/0004-6361/202243940.
7. Godoy-Rivera, D.; Nitschelm, C.; Oravetz, A.; Pan, K.; Roman-Lopes, A. Close substellar-mass companions in stellar wide binaries. *Monthly Notices of the Royal Astronomical Society* **2021**, *509*, 3355–3364. https://doi.org/10.1093/mnras/stab3095.
8. Mamajek, E.E.; Hillenbrand, L.A. Improved Age Estimation for Solar-Type Dwarfs Using Activity-Rotation Diagnostics. *The Astrophysical Journal* **2008**, *687*, 1264–1293. https://doi.org/10.1086/591785.
9. Kendall, M.G. A New Measure of Rank Correlation. *Biometrika* **1938**, *30*, 81–93. https://doi.org/10.1093/biomet/30.1-2.81.